Development of nano Ni$_x$Mg$_y$O solid solutions with outstanding anti-carbon deposition capability for the steam reforming of methanol

Xiang Luo [a], Yu Hong [a], Fuchen Wang [b], Siqi Hao [c], Chengheng Pang [a], Edward Lester [d], Tao Wu [a,*]

[a] Key Laboratory of Clean Energy Conversion Technologies, The University of Nottingham Ningbo China, Ningbo 315100, PR China
[b] Institute of Clean Coal Technologies, East China University of Science and Technology, Shanghai 200237, PR China
[c] Department of Chemical and Environmental Engineering, The University of Nottingham Ningbo China, Ningbo 315100, PR China
[d] Department of Chemical and Environmental Engineering, The University of Nottingham, University Park, Nottingham NG7 2RD, UK

ARTICLE INFO

ABSTRACT

In this study, different types of nano Ni$_x$Mg$_y$O solid solutions for the steam reforming of methanol were prepared via three different preparation methods. The solid solutions were characterised systematically by using a suite of characterisation techniques. TEM analysis demonstrated that Ni particles in these solid solutions were in nano-scale with an average size of 9.6–12 nm. The catalytic performance of these catalysts was evaluated using a fixed-bed reactor operated under atmospheric pressure at four different temperatures, i.e., 400, 500, 600 and 700 °C, and at two steam-to-carbon ratios (S/C), i.e., S/C = 1 and 3. Results showed that the nano Ni$_x$Mg$_y$O material (Ni$_x$Mg$_y$O-hydro), which was prepared using a hydrothermal method, achieved the highest methanol conversion efficiency of 97.4% and hydrogen yield of 58.5% under a S/C ratio of 3. The evaluation on carbon deposition resistance showed that nano Ni$_x$Mg$_y$O-hydro had no detectable carbon deposited under a S/C ratio of 3. In addition, physical and chemical properties of these catalysts were also studied by using H$_2$-Temperature-Programmed Reduction/Desorption(H$_2$-TPR/D), CO$_2$-Temperature- Programmed Desorption(CO$_2$-TPD) and X-ray Photoelectron Spectroscopy(XPS). The outstanding carbon deposition resistance of Ni$_x$Mg$_y$O-hydro was attributed to the "isolation effect" of the Ni$_x$Mg$_y$O solid solution structure, which restricts Ni nano particles from aggregation. The high basicity of the surface of Ni$_x$Mg$_y$O-hydro catalyst also resulted in the enhanced adsorption of CO$_2$ and therefore contributed to anti-carbon deposition by providing oxygen to promote the gasification reaction between carbon and CO$_2$.

© 2016 Elsevier B.V. All rights reserved.

1. Introduction

In the past few decades, energy consumption increased rapidly worldwide, especially in emerging countries such as China and India [1]. However, the use of fossil fuels to meet the increasing energy demand has already led to severe environmental problems, such as global warming and poor air quality [2]. Since 1990s, as a clean energy carrier, hydrogen, has attracted significant attention globally due to its high energy density, high conversion efficiency and environmental-friendly nature [3]. Currently, hydrogen is produced commercially via processes such as catalytic reforming of natural gas, partial oxidation of heavy oil and coal gasification, etc. [4].
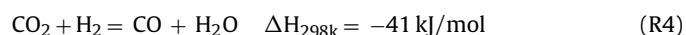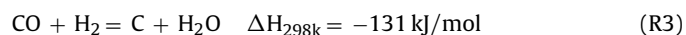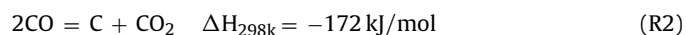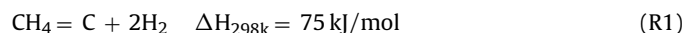
To date, significant amount of work has been carried out to develop catalysts for hydrogen production through catalytic reforming of a variety of raw materials, such as natural gas, biomass, bio-oil and alcohols [5–9]. Among the transition metal catalysts being studied, Ni-based catalysts have been studied extensively due to their high catalytic performance in the steam reforming of oxygenated hydrocarbons and low cost, which make these catalysts widely used commercially [10–12]. However, the use of Ni-based catalysts is usually associated with problems during the steam reforming process, such as deactivation of catalysts and reactor occlusion due to oxidation, sintering, and poor carbon resistance [13].

Generally, carbon deposition occurs via following reactions: hydrocarbon decomposition (R1), CO disproportionation (R2) and

CO hydrogenation (R3) [14]. However, both (R2) and (R3) are accompanied by reverse water-gas shift reaction (R4) [14,15].

$$CH_4 = C + 2H_2 \quad \Delta H_{298k} = 75\ kJ/mol \tag{R1}$$

$$2CO = C + CO_2 \quad \Delta H_{298k} = -172\ kJ/mol \tag{R2}$$

$$CO + H_2 = C + H_2O \quad \Delta H_{298k} = -131\ kJ/mol \tag{R3}$$

$$CO_2 + H_2 = CO + H_2O \quad \Delta H_{298k} = -41\ kJ/mol \tag{R4}$$

Normally, carbon deposition during reforming process can be suppressed by introducing more steam into the reaction system to promote reverse reactions of (R3) and (R4) to form more CO_2 and less CO, which subsequently inhibits (R2). However, the penalty of such is the increased energy consumption due to the endothermic property of reverse reactions of (R3) and (R4) and the excessive amount of unreacted steam in the reaction system. Another approach to mitigate carbon deposition is to use noble metals such as Pt, Pd, Rh and Ag as active component(s) in the catalysts, which could alleviate the aggregation of Ni particles and subsequently lower the rate of carbon formation [16,17]. The doping of rare earth elements in reforming catalysts was also found effective in inhibiting carbon deposition [18–20]. It is reported that CeO_2 in the catalyst could provide lattice oxygen for coke removal due to its unique redox properties and high oxygen capacities [18,19]. The basic La_2O_3 was also found effective in the activation of CO_2 to remove surface carbon species [20]. In addition, low acidity was found suppress carbon formation via the inhibition of direct decomposition of hydrocarbons [21]. Therefore, alkali or alkali earth elements, such as B, K, Mg and Ca, are often added into alumina catalysts to adjust surface acidity of the catalysts [22–24].

It was also reported that the basic MgO showed high resistance ability for carbon deposition due to its ability to activate CO_2 [25,26]. The high melting point of MgO (3073 °C) contributes to the thermal stability of the catalysts and enables the reaction take place under its hutting temperature, at which metal atoms gain sufficient energy to escape slowly from surface of the crystal [27]. However, the low specific surface area and low catalytic activation of the Ni/MgO catalyst restricted its further development and applications. The Ni_xMg_yO solid solutions have been widely studied and have been proved highly effective for the catalytic reforming of natural gas [28–31]. However, not much work has yet been carried out to understand the catalytic performance of Ni_xMg_yO solid solutions in the steam reforming of methanol, and how preparation methods affect the structure of these nano solid solutions and subsequently influence their catalytic performance and anti-carbon deposition capability.

In this study, the main purpose was to develop nano Ni_xMg_yO solid solutions with high catalytic performance and outstanding anti-carbon deposition property for the steam reforming of methanol. Different preparation methods were adopted to prepare nano Ni_xMg_yO solid solutions with different structures. These catalysts were then tested to evaluate their catalytic performance as well as the propensity in carbon deposition. Fresh and spent catalysts were also characterised to understand the differences in catalytic performance and to reveal the mechanism for the inhibition of carbon deposition.

2. Materials and experimental methods

2.1. Preparation of catalysts

All the chemicals used in this research were analytical grade purchased from Sinopharm Chemical Reagent Co., Ltd. (Shanghai, China).

In this study, three different nano Ni_xMg_yO solid solutions were prepared using three different methods. The preparation of the first type of Ni_xMg_yO catalyst started from the preparation of MgO support by precipitation of $Mg(NO_3)_2 \cdot 6H_2O$ with ammonia at room temperature followed by drying in air at 105 °C for 12 h and calcination in air at 600 °C for 4 h. The catalyst containing 10 wt% nickel in Ni_xMg_yO solid solution was achieved via incipient wetness impregnation (IWI) using aqueous solution of $Ni(NO_3)_2 \cdot 6H_2O$ impregnated onto the MgO support at room temperature. The catalyst was subsequently dried at 105 °C for 12 h, and then calcined in air at 600 °C for 4 h. This catalyst was denoted as Ni_xMg_yO-impre.

The second type of Ni_xMg_yO catalyst was prepared by following a similar procedure as described previously. The only difference was the added hydrothermal treatment of the catalysts at 100 °C for 24 h after precipitation. This catalyst was denoted as Ni_xMg_yO-hydro.

The third type of Ni_xMg_yO catalyst was prepared by co-precipitation of $Mg(NO_3)_2 \cdot 6H_2O$ and $Ni(NO_3)_2 \cdot 6H_2O$ in an ammonia solution at a controlled concentration, followed by aging at 40 °C for 6 h. The aged mixture was then dried in air at 105 °C for 12 h, calcined in air at 600 °C for 4 h, and treated hydrothermally following the same hydrothermal process as the preparation of Ni_xMg_yO-hydro. This catalyst was denoted as Ni_xMg_yO-copre.

In addition, 10 wt% Ni/γ-Al_2O_3 was prepared for comparison purpose using incipient wetness method. The γ-Al_2O_3 support was purchased from V-SK Co., Ltd., which had a BET surface area around 200 m^2/g. Before the impregnation process, the alumina support was calcined at 600 °C for 8 h to remove its surface contaminants. The impregnation was conducted under room temperature. The sample was then dried at 105 °C for 12 h and calcined in oxidizing atmosphere at 600 °C for 4 h. This catalyst was denoted as Ni_xAl_yO.

2.2. Catalytic performance test

The tests of catalytic performance were carried out in a fixed-bed reactor (I.D. = 12 mm) under atmospheric pressure. The fresh catalyst (approximately 0.5 g) was diluted with quartz sand (8 g, Ø 2–3 mm; Aladdin) and placed into the reactor on top of a layer of quartz wool. Prior to each test, the catalyst was reduced in situ with 25 vol% of H_2 in N_2 at a flow rate of 400 ml/min at 600 °C for 1 h.

A mixture of water and methanol was pumped into the testing rig at a flow rate of 1 ml/min (1 atm, room temperature) by using a liquid piston pump (Eldex Lab, Inc) with a reproducibility of ±0.3%. The pump was calibrated prior to each test and maintained frequently to ensure its repeatability and accuracy. Before being fed into the catalytic reactor, the liquid mixture was evaporated in a preheater at 300 °C. Water and methanol mixture with two molar ratios (S/C = 1 and 3) were adopted in this study, together with two different gas hourly space velocities (GHSV, 92,000 ml/(g_{cat}·h) and 114,000 ml/(g_{cat}·h)). After passing through a cold trap, the effluent was collected by using a 1 l Tedlar bag and analysed using an off-line Gas Chromatograph (GC-2014, SHIMADZU) equipped with 2 thermal conductivity detectors (TCD) and 1 hydrogen flame ionization detector (FID). In each test, N_2 gas at a flow rate of 300 ml/min was used in the reaction system as a carrier gas. The flow rate of product gas (H_2, CO_2, CO and CH_4) was calculated based on the known flow rate of N_2 and their relative concentration to N_2, which was analysed by using the GC. The calculation of methanol conversion was based on the flow rate of methanol introduced to the reaction system and the corresponding carbon balance. The concentration of other gases detected by the FID, such as ethane, was always very low and was therefore neglected. The methanol conversion, the selectivity of CO formation, the selectivity of CH_4 formation, H_2 yield and the H_2/CO ratio were determined by using following formulae [32,33]:

$$CH_3OH\ conversion\ (\%) = \frac{[CO_2]_{out} + [CH_4]_{out} + [CO]_{out}}{[CH_3OH]_{in}} \times 100\% \tag{1}$$

$$CO \text{ selectivity} (\%) = \frac{[CO]_{out}}{[CO_2]_{out} + [CH_4]_{out} + [CO]_{out}} \times 100\% \qquad (2)$$

$$CO_2 \text{ selectivity} (\%) = \frac{[CO_2]_{out}}{[CO_2]_{out} + [CH_4]_{out} + [CO]_{out}} \times 100\% \qquad (3)$$

$$CH_4 \text{ selectivity} (\%) = \frac{[CH_4]_{out}}{[CO_2]_{out} + [CH_4]_{out} + [CO]_{out}} \times 100\% \qquad (4)$$

$$H_2 \text{ yield} (\%) = \frac{[H_2]_{out}}{[CH_3OH]_{in} \times 3} \times 100\% \qquad (5)$$

$$H_2/CO \text{ ratio} = \frac{[H_2]_{out}}{[CO]_{out}} \% \qquad (6)$$

2.3. Characterization

2.3.1. N2 adsorption-desorption

Texture structure of the samples were characterised by using a Micrometrics ASAP-2020. In each analysis, approximately 200 mg of the catalyst was degassed at 300 °C for 5 h under high vacuum to remove moisture and other adsorbed gases. Specific surface area of the sample was calculated following the BET method and the pore size distribution was estimated following the BJH method. Details of these methods were described elsewhere [34].

2.3.2. X-ray diffraction

Powder X-ray diffraction (XRD) spectrum were acquired by using a Bruker D8 Advance with a Cu X-ray tube (λ = 1.5406 Å) operated at 40 kV and 40 mA. The 2θ was scanned from 10° to 90° (with a resolution of 0.01°). A standard procedure [35] was adopted in this study.

2.3.3. H2-temperature programmed reduction/desorption (H2-TPR and H2-TPD)

The H2-TPR and H2-TPD were carried out in a temperature-controlled micro-reactor, which was connected to a TCD (Finetec, Finesorb 3010D). In the TPR analysis, approximately 30 mg of the fresh catalyst was placed inside a U-shape quartz tube. The catalyst was then heated to 300 °C in argon at a flow rate of 20 ml/min and kept isothermal for 1 h and then cooled down to ambient temperature. The catalyst was then heated from room temperature to 950 °C at a heating rate of 5 °C/min in reducing atmosphere (10 vol% H2 in argon). H2 consumption was monitored by using an online TCD. Prior to TPD analysis, the catalyst was reduced in hydrogen at 600 °C for 4 h. During the desorption process, temperature was raised to 800 °C in argon at a heating rate of 5 °C/min.

2.3.4. CO2-temperature programmed desorption (CO2-TPD)

The CO2-TPD experiment was carried out in the device used previously for H2-TPD/TPR tests. Around 50 mg of catalyst was reduced at 600 °C for 4 h in a gas mixture of 10 vol% of H2 in argon. In the CO2-TPD experiment, CO2 (99.999 vol%) was introduced into the reactor at room temperature for 30 min. The gas was then switched to argon at a flow rate of 20 ml/min to purge off the residual CO2 in the reactor and the free CO2 on the surface of the catalyst. After signal of the TCD became stable, temperature was then raised to 600 °C to allow desorption to occur.

2.3.5. High resolution transmission electron microscopy (HRTEM)

Morphology of the fresh and spent catalysts was characterised by using a high-resolution transmission electron microscope (HRTEM; JEM-2100F, JEOL, Japan, 200 kV). The samples were dispersed into ethanol, and then transferred onto a copper grid prior to HRTEM analysis. Size distribution of Ni particles was determined by the manual measurement of more than 100 particles extracted from several TEM images.

2.3.6. Thermogravimetric analysis (TGA)

The amount of carbon deposited on catalyst was quantified by using a NETZSCH thermogravimetric analyser (STA449 F3). Approximately 10 mg of spent catalyst was heated in air from room temperature to 900 °C at a heating rate of 10 °C/min to allow carbon deposited on the catalyst to be burnt off.

2.3.7. Temperature programmed hydrogenation (TPH)

Carbon species deposited on spent catalysts was also characterised by temperature-programmed hydrogenation (TPH). The spent catalyst was purged with argon at 150 °C for 1 h and cooled down to ambient temperature. Prior to hydrogenation, the gas was switched to 10 vol% of H2 in argon at a flow rate of 20 ml/min. The temperature was then raised from room temperature to 950 °C at a heating rate of 5 °C/min. The online TCD was used to continuously monitor the composition of gas at the outlet.

2.3.8. Raman spectroscopy

Raman spectra from 1000 to 2000 cm^{-1} at ambient temperature were recorded by using a Renishaw inVia-reflex equipped with a 532 nm-wavelength laser. Each catalyst was analysed more than 3 times at different positions.

2.3.9. X-ray photoelectron spectroscopy

X-ray photoelectron spectroscopy (XPS) was also used to study the oxidation states of nickel species on the surface of catalysts. The fresh and spent catalysts were analysed by using a Shimadzu Axis Ultradld spectroscope operated under room temperature and a vacuum condition of 10^{-9} Torr [36].

3. Results and discussion

3.1. XRD analysis

XRD patterns of the fresh, reduced and spent catalysts are shown in Fig. 1. From the XRD spectrum, it is clear that the nickel crystal had peaks close to that of the MgO crystal. This was due to their identical lattice type and similar ionic radius value [37]. The peaks of nickel phase have increments of 0.6°, 0.8° and 0.81°, compared with peaks of MgO at $2\theta \approx$ 62.64°, 75.00°, and 79.00° [29]. In Fig. 1(B)–(D), no double structure was found associated with the five major peaks, which were assigned as MgO at 37°, 43°, 62°, 75° and 79° [30]. This proves the formation of Ni$_x$Mg$_y$O solid solution in all three Ni$_x$Mg$_y$O systems as a result of the excellent mutual solubility of these two metal oxides [29,30,37,38].

Compared the XRD spectra of the fresh, reduced and spent catalysts of these three Ni$_x$Mg$_y$O catalysts, no noticeable difference was found except some small changes in peak intensity. This demonstrated the outstanding thermal stability of Ni$_x$Mg$_y$O solid solutions prepared in this study. In addition, no peaks of metallic Ni (2θ = 44.6°, 51.3° and 76.1°) were identified for all the reduced and spent catalysts of Ni$_x$Mg$_y$O-copre, Ni$_x$Mg$_y$O-hydro and Ni$_x$Mg$_y$O-impre [39]. These results suggested that oxidized nickel particles in MgO matrix were not reduced to elemental Ni after the reduction process at 600 °C. Even after the 20 h durability tests, Ni particles were still fixed inside the MgO matrix. The main reason for this is the strong metal support interaction effect (SMSI) of Ni$_x$Mg$_y$O solid solution [39]. For Ni$_x$Al$_y$O catalyst (Fig. 1(A)), both γ-Al$_2$O$_3$ and NiAl$_2$O$_4$ were identified from the XRD spectra of the catalyst [40,41]. The 3 characteristic peaks for metallic Ni particles were detected in both reduced and spent catalysts. This result indicates that the bonding crystal force inside the Ni$_x$Mg$_y$O solid solution is stronger than that of Ni$_x$Al$_y$O structure. The Ni particles in Ni$_x$Al$_y$O structure normally contribute to the activation of catalysts at the initial stage of the reaction. Due to the weak bonding force, these
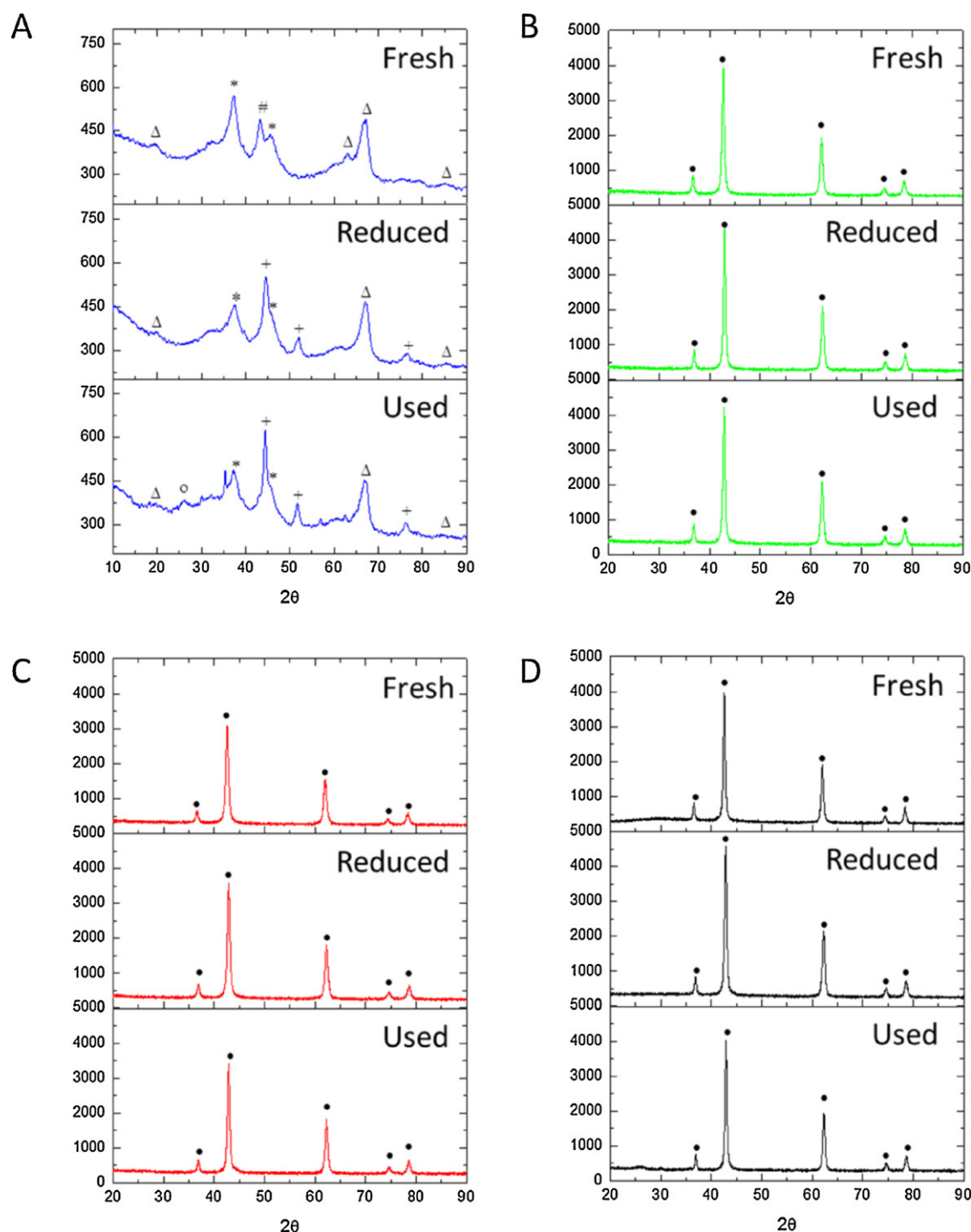
Fig. 1. X-ray diffraction patterns of fresh, reduced and spent catalysts (A) Ni_xAl_yO, (B) Ni_xMg_yO-copre, (C) Ni_xMg_yO-hydro, (D) Ni_xMg_yO-impre, $\triangle$: γ-Al_2O_3; *: $NiAl_2O_4$; +: Ni; #: NiO; $\bigcirc$: ordered carbon; ●: NiO/MgO.

free Ni particles could overcome the surface crystal forces and aggregate to form larger size Ni crystallites during the reforming process, which would worsen carbon deposition issues and accelerate the deactivation of the catalysts. Based on XRD analysis, it can therefore be concluded that the Ni_xMg_yO solid solution might be more stable and show a better catalytic durability than the Ni_xAl_yO catalyst. For the spent Ni_xAl_yO catalyst, a small peak around 26.6°, which was attributed to the formation of ordered carbon, was also detected [42,43]. This indicates that severe carbon deposition occurred on the surface of the Ni_xAl_yO catalyst.

3.2. N_2 physiosorption analysis

From Fig. 2(A), it can be seen that the sorption isotherm of Ni_xAl_yO catalyst was Type IV. Its big hysteresis loop was associated with capillary condensation in mesopores (>2 nm and <50 nm) and the large surface area [44]. From Fig. 2(B), it is clear that its pore width varied between 1.9 nm and 31.7 nm. The isotherm curves of the other three catalysts can be categorized as Pseudo-Type II isotherm. This type of isotherm indicates that slit-shaped pores or aggregates of platy particles existed on these catalysts [45]. It is
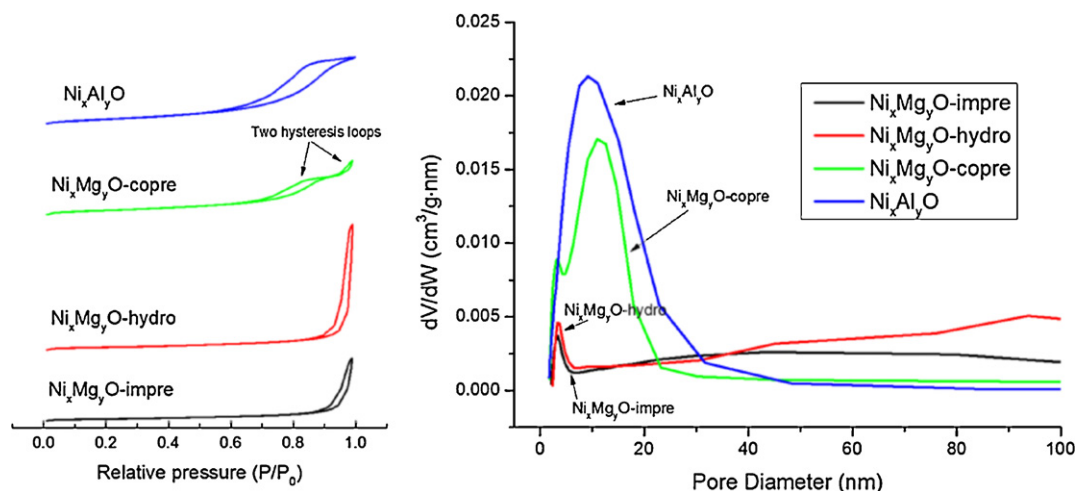
Fig. 2. (A) N_2 physisorption isotherms of fresh catalysts; (B) pore size distribution of fresh catalysts.

Table 1
N_2 physisorption analysis results of both reduced and spent catalysts.

Catalyst	State	Surface area (m^2/g)	Total pore volume (cm^3/g)	t-plot micropore volume (cm^3/g)
Ni_xMg_yO-impre	Reduced	49.7	0.343	0.00469
	Spent	53.5	0.295	0.00059
Ni_xMg_yO-hydro	Reduced	79.8	0.841	0.00657
	Spent	71.6	0.768	0.00511
Ni_xMg_yO-copre	Reduced	54.0	0.364	0.00392
	Spent	52.5	0.339	0.00189
Ni_xAl_yO	Reduced	131.4	0.372	0.00390
	Spent	108.7	0.313	0.00261

worth noting that there were two hysteresis loops on the sorption isotherm of Ni_xMg_yO-copre, which suggests that there were two types of pores with different sizes. This observation is consistent with the pore size distribution of Ni_xMg_yO-copre as shown in Fig. 2(B). The existence of both small pores (<2 nm) and mesopores in Ni_xMg_yO-copre could enhance the 'confined effect' to resist metallic Ni particles from sintering, which could then contribute to the mitigation of carbon deposition [34,46]. Textural structure of the reduced catalysts and the spent catalysts after 20 h testing was summarized in Table 1. Compared with Ni_xMg_yO-impre, the hydrothermal treatment resulted in a 60% increase in surface area, the highest total pore volume and micropore volume for Ni_xMg_yO-hydro. Normally, a larger surface area helps improve metal dispersion on the surface of the catalyst, and a higher micropore volume enhances the adsorption of reactants. These improvements subsequently contribute to a higher catalytic performance of the catalyst. The Ni_xMg_yO-copre had an even higher surface area and it could be attributed to its porous structure, which was confirmed by TEM analysis in Section 3.5. The alumina catalyst showed the highest surface area, due to its typical mesostructure.

Normally, apart from surface area and total pore volume, micropore volume is another key factor associated with metallic agglomeration [47]. A higher micropore volume helps alleviate metallic agglomeration and enhances gaseous exchange, which subsequently promotes reforming process [36]. In Table 1, comparing the reduced catalysts with the spent catalysts, the dramatic decrease in micropore volume of Ni_xMg_yO-impre from 0.00469 to 0.00059 cm^3/g suggests that the deactivation of the catalyst was due to its surface restructuring. However, for Ni_xMg_yO-hydro, no significant change in micropore volume was observed. This suggests that this catalyst was more durable and exhibited the least

morphology changes after long-time testing, which is further verified in Section 3.7.

3.3. H_2-TPR analysis

H_2-TPR experiment was conducted to investigate surface Ni species and the interactions between Ni species and the support materials. Fig. 3 shows the TPR profiles of calcined catalysts. It can be seen that the main peak of Ni species in Ni_xAl_yO was found to be at 792 °C, which is assigned as the temperature for oxidized Ni particles to be reduced from $NiAl_2O_4$ spinel [39]. The TCD signal at temperatures below 600 °C was weak. The TPR results verified the formation of $NiAl_2O_4$ spinel with a very small amount of free Ni species in the Ni_xAl_yO catalyst [48,49]. All the Ni_xMg_yO-copre, Ni_xMg_yO-hydro and Ni_xMg_yO-impre catalysts showed their strongest peaks at a temperature higher than 800 °C, which was ascribed as the temperature for the reduction of Ni cations from the Ni_xMg_yO solid solution [31]. The Ni cations were diffused into MgO lattice [50] for the three MgO based catalysts. Since the reduction temperature and the reforming test temperature were both 600 °C, this temperature was not high enough for oxidized Ni particles in the MgO matrix to be reduced. This is the reason why no noticeable peaks for metallic Ni were found from the XRD spectrums of the Ni_xMg_yO catalysts. However, low intensity peaks of Ni species were evident for the three Ni_xMg_yO catalysts in the temperature range of 450–650 °C. This suggests that Ni particles were highly dispersed under the MgO subsurface [38] and were in nano-scale. This is why these Ni species were not identified in previous XRD analysis, as described in Section 3.1. These highly dispersed nano-scale Ni particles could potentially contribute to the good catalytic reforming performance of these Ni_xMg_yO catalysts.
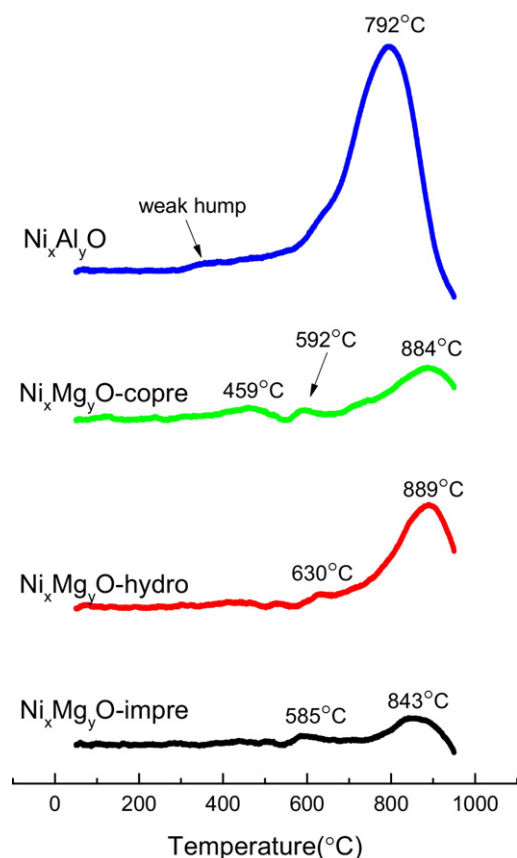
Fig. 3. H$_2$-temperature programmed reduction profiles of the fresh catalysts.

Fig. 4. H$_2$-TPD profiles of the reduced catalysts.

3.4. H$_2$-TPD analysis

H$_2$-TPD experiment was also carried out to investigate Ni species on the reduced catalysts after 4 h hydrogen reduction at 600 °C. Two types of hydrogen desorption peaks can be identified in Fig. 4. The temperature peak in the range of 150–300 °C is assigned as T$_L$, and the peak in the range of 300 –600 °C is assigned as T$_H$. It is generally believed that T$_L$ corresponds to the existence of large Ni particles on the surface or subsurface, and T$_H$ indicates the presence of small Ni particles in the subsurface [31]. It can be seen from Fig. 4 that the main peak of Ni$_x$Al$_y$O catalyst located at 248 °C, with a high intensity and a narrow width. This suggested the existence of large Ni crystallites on the surface of the support of Ni$_x$Al$_y$O, which were larger than Ni particles in Ni$_x$Mg$_y$O. The strong peaks for Ni$_x$Mg$_y$O catalysts suggested the Ni crystallites did exist on the subsurface of the catalysts and were in much smaller size. This further confirmed the existence of nano-scale Ni particles, which is consistent with what was found based on TPR tests. It is speculated that these nano-scale Ni particles are highly dispersed in the MgO matrix. The strong interactions between Ni particles and MgO resulted in an 'isolation effect' to prevented Ni aggregation from happening [21]. These would then contribute to the outstanding catalytic performance, carbon deposition resistance and stability of these Ni$_x$Mg$_y$O solid solutions. In summary, H$_2$-TPD analysis demonstrated that different Ni$_x$Mg$_y$O solid solutions had Ni particles in different size ranges and dispersed in MgO in different patterns. These different structures would result in different accessibility of Ni particles for steam reforming and subsequently lead to difference in catalytic performance of these Ni$_x$Mg$_y$O solid solutions.
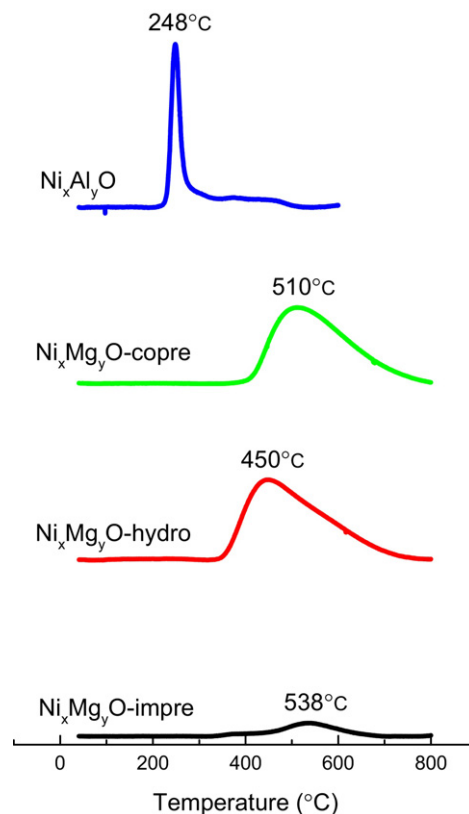
3.5. TEM analysis

The TEM images of catalysts studied are shown in Fig. 5. The Ni$_x$Al$_y$O catalyst, as shown in Fig. 5(A), had an average metal particle size around 14.8 nm (as shown in Table 2), which is in consistence with what was reported by others [51,52]. The analogy in terms of morphology between Ni$_x$Mg$_y$O-impre and Ni$_x$Mg$_y$O-hydro was also observed, which was attributed to their similar synthesis procedure. The MgO particles were all sub-nanoparticles, which are smaller than 200 nm. The average size of Ni particles in Ni$_x$Mg$_y$O-hydro was 10.1 nm, which is slightly larger than Ni particles in Ni$_x$Mg$_y$O-impre (average size 9.6 nm). The Ni$_x$Mg$_y$O-copre catalyst also demonstrated porous MgO nanosheets with an average Ni particle size of 12.0 nm, which is very similar to the earlier work conducted by Zhu et al. [53]. Due to the largest Ni crystallites in Ni$_x$Al$_y$O, it would result in poor carbon deposition resistance, whilst Ni$_x$Mg$_y$O-hydro had the smallest Ni particle size and was expected to show better carbon deposition resistance.

The metal dispersion (D$_M$) was also calculated based on the size of particles determined from TEM images using Vannice's equation [54]:

$$D_M = 6 \times 10^7 \frac{V_M}{A_M} \frac{1}{d\,(nm)} \qquad (7)$$

Where d is the average diameter of a metal particle in nm, V_M is the bulk atomic volume of metals (for Ni, $V_M = 1.10 \times 10^{-23}$ cm^3), A_M is the area of an atom (for Ni, $A_M = 1.0 \times 10^{-15}$ cm^2) [55]. Metal dispersion of materials is shown in Table 2. It can be seen that different preparation methods resulted in the difference in Ni dispersion in different Ni$_x$Mg$_y$O solid solutions. Since Ni$_x$Mg$_y$O-impre and Ni$_x$Mg$_y$O-hydro had relatively higher metal dispersion, it was expected that these two catalysts would have better catalytic performance as well as anti-carbon deposition property than the other catalysts.
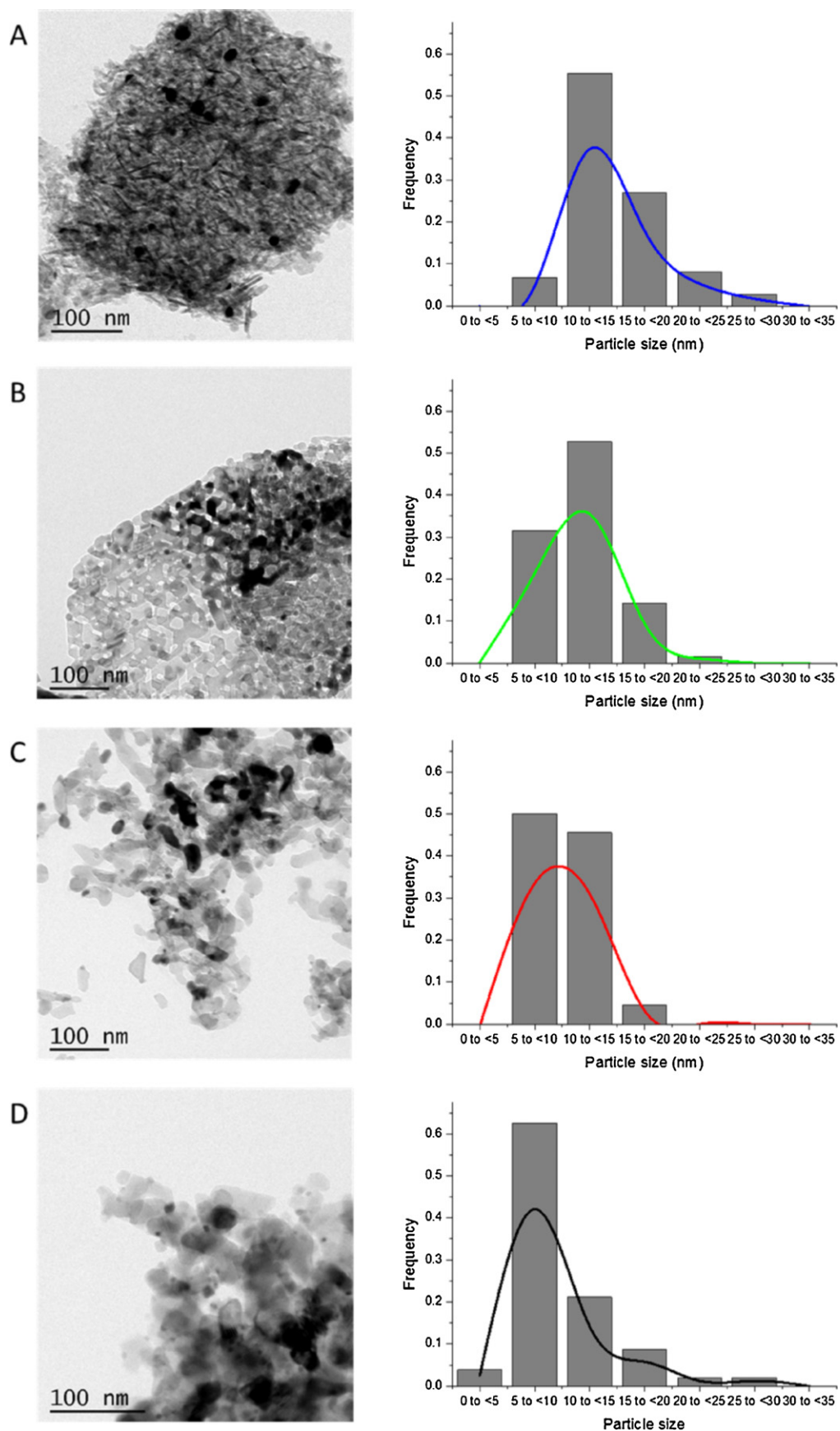
Fig. 5. TEM images and Ni particle size distribution of reduced catalysts (A) Ni_xAl_yO, (B) Ni_xMg_yO–copre, (C) Ni_xMg_yO–hydro, (D) Ni_xMg_yO–impre.

Table 2
Metal particle size and dispersion from TEM for both fresh and spent catalysts.

Catalyst	Ni particle size of fresh catalyst (nm)	Ni Particle size of spent catalyst (nm)	Particle size increment (%)	Ni dispersion fresh catalyst (%)
Ni_xMg_yO-impre	9.6	20.2	110.4	6.9
Ni_xMg_yO-hydro	10.1	15.1	49.5	6.6
Ni_xMg_yO-copre	12.0	13.4	11.7	5.5
Ni_xAl_yO	14.8	24.8	67.6	4.5
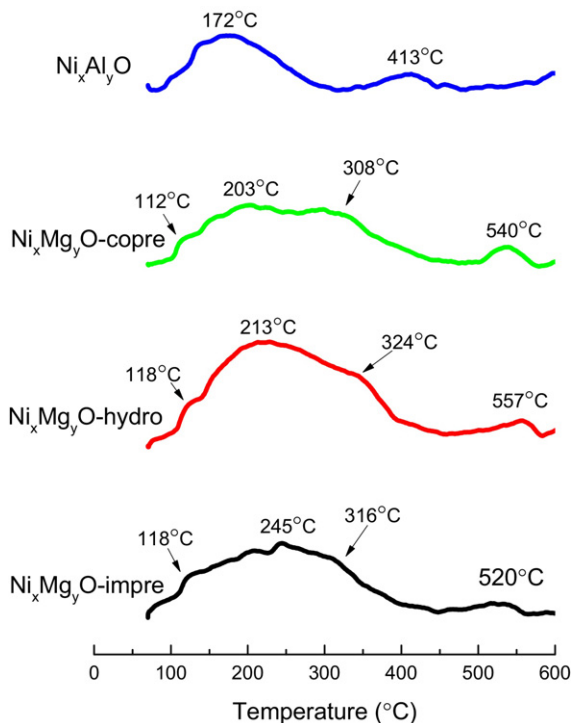
Fig. 6. CO$_2$-TPD profiles of the reduced catalysts.

3.6. CO$_2$-TPD analysis

Normally, CO$_2$-TPD analysis can show the strength of Lewis basicity and the number of basic sites on the surface of the catalysts [56,57]. Theoretically, more basic sites on the surface of the catalyst could promote the chemisorption of CO$_2$, which accelerates the reverse Boudouard reaction (C + CO$_2$ → 2CO). On the other hand, the excessive CO$_2$ on the surface could also suppress the adsorption of CH$_4$ and CO, which subsequently hinders carbon formation via the decomposition of methane (R1) and CO hydrogenation (R3).

The CO$_2$-TPD profiles of these catalysts are shown in Fig. 6. For individual catalysts, their desorption peaks present in two temperature ranges. The first peak for these Ni$_x$Mg$_y$O catalysts was in a broad low temperature range from 100 to 450 °C, which was associated with the weak basic sites [58,59]. Their second desorption peak located at a temperature above 500 °C, which was assigned as moderate basic sites. For Ni$_x$Al$_y$O catalyst, the first desorption temperature was in the range of 100 –300 °C, and the moderate basic site peak shifted to a lower temperature (413 °C). According to the area of these peaks, the total basicity of these catalysts was found in the order of Ni$_x$Mg$_y$O-hydro > Ni$_x$Mg$_y$O-impre > Ni$_x$Mg$_y$O-copre > Ni$_x$Al$_y$O, which suggests that Ni$_x$Mg$_y$O-hydro would show the best carbon deposition resistance by promoting CO$_2$ adsorption to enhance reverse Bourdard Reaction and to suppress (R1) and (R3).

Table 3
Methanol conversion and H$_2$ yield after 20 hours' steam reforming at different steam carbon ratios.

	Steam-to-carbon ratio	Methanol conversion	H$_2$ yield
Ni_xMg_yO-impre	3	55.3%	30.0%
Ni_xMg_yO-hydro	3	97.4%	58.5%
Ni_xMg_yO-copre	3	66.2%	38.0%
Ni_xAl_yO	3	97.1%	61.6%
Ni_xMg_yO-impre	1	51.4%	29.0%
Ni_xMg_yO-hydro	1	58.3%	33.8%
Ni_xMg_yO-copre	1	57.5%	33.6%
Ni_xAl_yO	1	51.1%	28.8%

3.7. Catalytic performance

It can be seen from Fig. 7(A) that the conversion efficiency increased with the increase in temperature for each catalyst. The Ni$_x$Al$_y$O exhibited the highest conversion efficiency of 24.1% at 400 °C, and reached 100% conversion at 600 °C. The Ni$_x$Mg$_y$O-hydro had a higher initiation temperature for catalytic reforming compared with Ni$_x$Al$_y$O, which could be attributed to its higher reduction temperature. The Ni$_x$Mg$_y$O-impre and Ni$_x$Mg$_y$O-copre showed similar methanol conversion, which was much lower than that of Ni$_x$Al$_y$O catalysts. Their low performance at low temperatures could be attributed to the lower reducibility as shown in TPR tests, which suggested that less amount of Ni particles was reduced. The H$_2$-TPD results also indicated most Ni species dissolved deeply inside the MgO matrix and subsequently left only a small amount of Ni particles at the subsurface (H$_2$ desorption peak temperature >500 °C) to participate in the reforming reaction. However, when the reaction temperature was raised to 700 °C, all three Ni$_x$Mg$_y$O catalysts achieved 100% methanol conversion. The reason could be that, at high temperatures, the kinetic energy of methanol molecules was high enough to diffuse deeper into the Ni$_x$Mg$_y$O matrix. Thus, more oxidized Ni particles at the deeper layers of the Ni$_x$Mg$_y$O catalysts could be reduced and become available for catalytic reactions. The H$_2$ yield, as shown in Fig. 7(B), is consistent with methanol conversion efficiency. High temperature (>600 °C) favored H$_2$ production via methanol decomposition and carbon gasification reactions. In Fig. 7(C), the H$_2$/CO ratio decreased with the increase in temperature. The reason for this was that high temperature favored both reverse water-gas shift reaction (R4) and reverse Boudouard reaction (C + CO$_2$ → 2CO), which would lead to an excessive yield of CO [27,60]. Fig. 7(D) shows the selectivity of both CO and CO$_2$ at 600 °C for the 4 catalysts. All the three Ni$_x$Mg$_y$O catalysts showed higher CO yield and lower CO$_2$ yield compared with the Ni$_x$Al$_y$O catalyst. It might be due to the higher CO$_2$ capture ability of Ni$_x$Mg$_y$O solid solution, which resulted in a greater amount of CO$_2$ being adsorbed, and subsequently accelerated the reverse Boudouard reaction and mitigated carbon deposition. Therefore, the CO$_2$/CO ratio also demonstrated carbon inhibition phenomenon of these Ni$_x$Mg$_y$O catalysts.

The durability tests of these catalysts were also carried out at two different S/C ratios. The methanol conversion efficiency and H$_2$ yield after 20 hours' testing were shown in Table 3 and Fig. 8. In this study, the S/C ratio was 3 and the flow rate of methanol was kept as 0.86 ml/(g$_{cat}$·min) (GHSV at 114,000 ml/(g$_{ca·t}$h)). After 20 hours' testing, the Ni$_x$Mg$_y$O-hydro and Ni$_x$Al$_y$O still exhibited
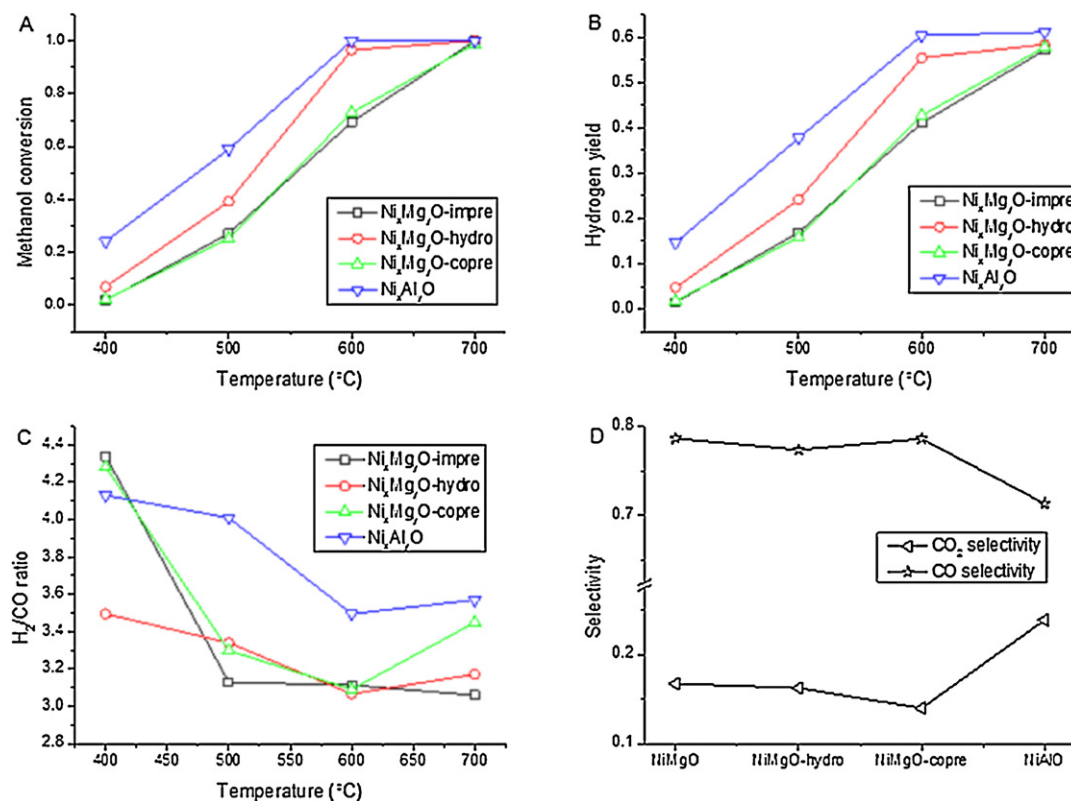
Fig. 7. Methanol steam reforming performance of the catalysts (reaction condition: P = 1 atm, GHSV = 114,000 ml/g·h, S/C = 3).
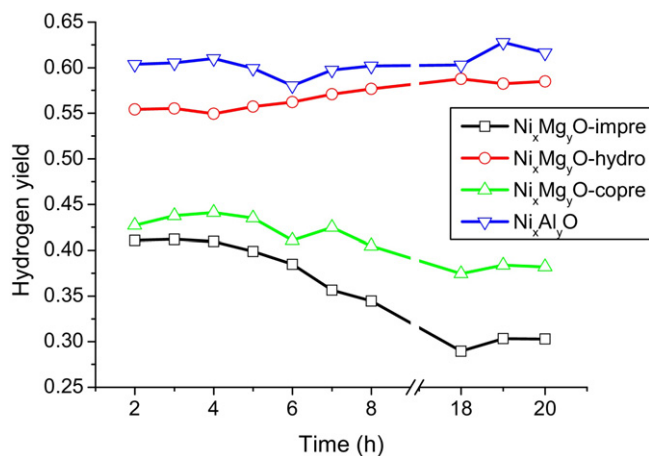

Fig. 8. H_2 yield for different catalysts (reaction condition: P = 1 atm, T = 600 °C, GHSV = 114,000 ml/g·h, S/C = 3).

outstanding stability with around 97% of methanol conversion and their hydrogen yield remained as 58.5% and 61.6%, respectively. For both the Ni_xMg_yO-hydro and the Ni_xAl_yO catalysts, the final H_2 yield increased compared with their initial yields as shown in Fig. 8. This observation could be attributed to the gradual reduction of oxidized Ni particles from the MgO matrix and the $NiAl_2O_4$ spinel during the reforming process.

However, it was also observed in this study that methanol conversion of the Ni_xMg_yO-impre and the Ni_xMg_yO-copre decreased by 14.1% and 6.7% respectively compared with their corresponding fresh catalysts. The reason for the deactivation could be the slow surface restructuring, which altered the chemisorption behaviour on the surface of the catalysts or the number of active sites. This conclusion is also supported by the BET results, which showed that

t-plot micropore volume of these two catalysts decreased significantly. The micropore volume of the spent Ni_xMg_yO-copre was less than half of its fresh catalyst. For the Ni_xMg_yO-impre catalyst, the micropore volume decreased significantly from 0.00469 to 0.00059 cm^3/g. The catalytic performance of the Ni_xMg_yO-hydro was compared with catalysts by other researchers [61–65] and summarized in Table 4. The commonly used catalysts for the steam reforming of methanol were Cu-based and were used at temperatures below 300 °C. It can be seen that only the La_2CuO_4 catalyst showed similar performance Ni_xMg_yO-hydro prepared in this study. The other catalysts and the two commercial catalysts were not as good as Ni_xMg_yO-hydro in terms of methanol conversion. Compared with the two layers of $Ni/Ce-ZrO_2$ and Ni/YSZ catalysts, which achieved a hydrogen yield of 51.0% at 700 °C after 10 hours' testing, and 58.6% at 750 °C [66], the Ni_xMg_yO solid solution developed in this study also showed better performance (hydrogen yield 58.5% at 600 °C). In terms of hydrogen production activity, Ni_xMg_yO-hydro showed the highest rate, which again proved the outstanding performance of this catalyst.

In order to investigate performance under harsh operating conditions and to understand carbon deposition resistant ability of these catalysts, tests were also conducted at a low S/C ratio (S/C = 1) and a much higher methanol input rate (1.38 ml/(g_{cat}·min), GHSV at 92,000 ml/(g_{cat}·h)). The methanol conversion and hydrogen yield were listed in Table 3. Under these conditions, the conversion efficiency of all the catalysts was lower than 60% after 20 hours' testing. The lowest conversion was found for Ni_xAl_yO (51.1%) and was associated with severe carbon deposition (28.8 wt% carbon deposition in total). The Ni_xMg_yO-hydro, which had a high total basicity, kept its high catalytic activity with good carbon resistance ability (1.5 wt% carbon deposition in total). The better performance of Ni_xMg_yO-copre compared with Ni_xMg_yO-impre could be attributed to its moderate increase in the size of Ni particle by 11.7%, while the size of metal particle of Ni_xMg_yO-impre increased by

Table 4
Comparison of catalytic performance of different catalysts.

Catalyst	Temperature (°C)	Methanol conversion (%)	Activity ($\mu molH_2/(g_{cat}\,s)$)	Hydrogen yield (%)
Cu/Zn/Al [61]	260	76	203	–
La_2CuO_4 [63] (nanofiber or powder)	400	100	280	–
Cu/Zn/Al2O3 [64] (commercial)	260	60	–	–
Cu/Zn/Al2O3 [65] (commercial)	300	57	–	–
Ni/Ce-ZrO$_2$ + Ni/YSZ [66]	700	–	–	51.0
Ni_xMg_yO-hydro	600	97	620	58.5

110.4%. Based on the results at S/C ratio = 1 and 3, Ni_xMg_yO-hydro was the best catalyst with better carbon deposition resistance and durability.

### 3.8. Characterization of the spent catalysts

3.8.1. TGA analysis

Normally, the burning of chars started at temperatures above 400 °C [67–69]. Therefore, in this study, the spent catalysts were heated in air to 900 °C to determine the quantity of carbon deposited on the catalysts, the results of which are presented in Table 5. When S/C = 3, Ni_xAl_yO experienced a moderate carbon deposition rate of 2.45 mg/g_{cat}·h although a conversion efficiency of 97.1% was achieved. This suggests a weak correlation between carbon deposition and the deactivation of the catalyst. For all Ni_xMg_yO catalysts, no carbon deposition was detected at 700 °C. This finding is better than what was reported by other researchers [66], in which 0.13 wt% of carbon was deposited at 700 °C. When S/C ratio was 1, the Ni_xMg_yO-hydro catalyst showed the lowest carbon deposition rate of 0.75 mg/(g_{cat}·h). This could be attributed to its high basicity and the excellent performance in steam reforming. Both the Ni_xMg_yO-impre and the Ni_xMg_yO-copre had slightly higher carbon deposition rates of 1.95 mg/(g_{cat}·h) and 2.10 mg/(g_{cat}·h), respectively. The Ni_xAl_yO catalyst exhibited the highest carbon deposition rate of 14.40 mg/(g_{cat}·h). It was reported [70,71] that basic supports supply more surface oxygen via CO_2 adsorption, which subsequently contributes to the removal of amorphous carbon. Fig. 9 shows the TGA-DSC profiles of the spent catalysts under a steam-to-carbon of 1. The peaks of DSC profile indicated that the burning temperature of the carbon species deposited on Ni_xAl_yO was higher than that of carbon formed on the MgO support. This also suggests that more highly ordered carbon formed on the Ni_xAl_yO catalyst [72].

3.8.2. Raman spectra

Raman spectra analysis was conducted to identify the types of carbon deposited on the spent catalysts. Fig. 10 shows the Raman spectra in 1000–2000 cm^{-1} region, together with the value of D/G ratio on the top left of the figure, in which the G band (1595 m^{-1}) was attributed to the highly ordered carbon, while the D band (1340 m^{-1}) was attributed to the disordered aromatic carbonaceous structure. Normally, highly ordered carbon species is less reactive and is difficult to be burned [73,74].

It can be seen that the Ni_xMg_yO-hydro had the highest D/G ratio, which means carbon deposited on this catalyst was of less highly
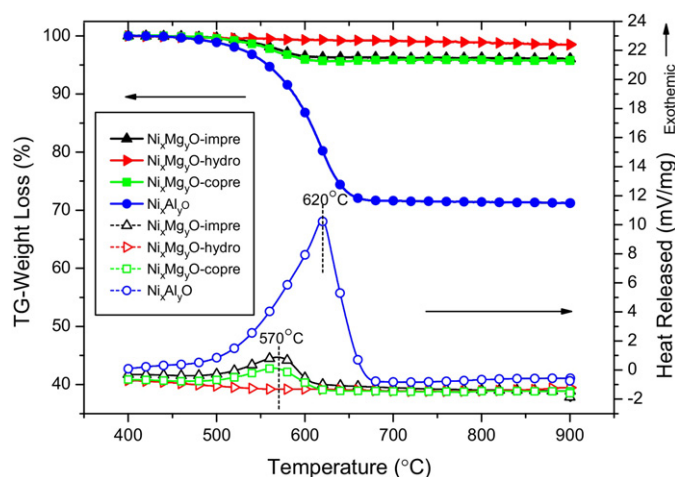
Fig. 9. TGA and DSC profiles of the spent catalysts after 20 h steam reforming (S/C = 1).

ordered carbon than the other three catalysts. Refer to the earlier study on carbon formation, the amorphous carbon, denoted as C_α and C_β, was formed initially via the direct decomposition of hydrocarbon or surface dissociation of carbonaceous gas [75]. These are amorphous carbon and are relatively reactive and could be burned via reacting with free oxygen near the surface of the catalysts. Once the rate of combustion of amorphous carbon is lower than the rate of formation, the amorphous carbon would start to accumulate on the surface of the catalyst and start to turn into highly ordered carbon, which is less reactive [75]. Due to the high basicity, surface of the Ni_xMg_yO-hydro had more free oxygen originated from adsorbed CO_2 or H_2O, which accelerated the combustion rate of the surface amorphous carbon and subsequantly suppressed the formation of highly ordered carbon during reforming process.

3.8.3. Temperature programmed hydrogenation

TPH analysis was also conducted in this study to distinguish different carbon species on the surface of spent catalysts. The results are illustrated in Fig. 11. Normally, carbon species with a hydrogenation temperature <300 °C is very reactive amorphous carbon (α-carbon) [34], which is more reactive than β-carbon with a hydrogenation temperature >600 °C [76]. Carbon species with a hydrogenation temperature greater than 800 °C is assigned as γ-carbon, which is highly unreactive [34,77].

Table 5
TGA analysis of the spent catalysts after 20 hours' testing.

Catalyst	Carbon deposition (mg/(g_{cat}·h)) at S/C = 3	Carbon deposition (mg/(g_{cat}·h)) at S/C = 1
Ni_xMg_yO-impre	ND[a]	1.95
Ni_xMg_yO-hydro	ND	0.75
Ni_xMg_yO-copre	ND	2.10
Ni_xAl_yO	2.45	14.40

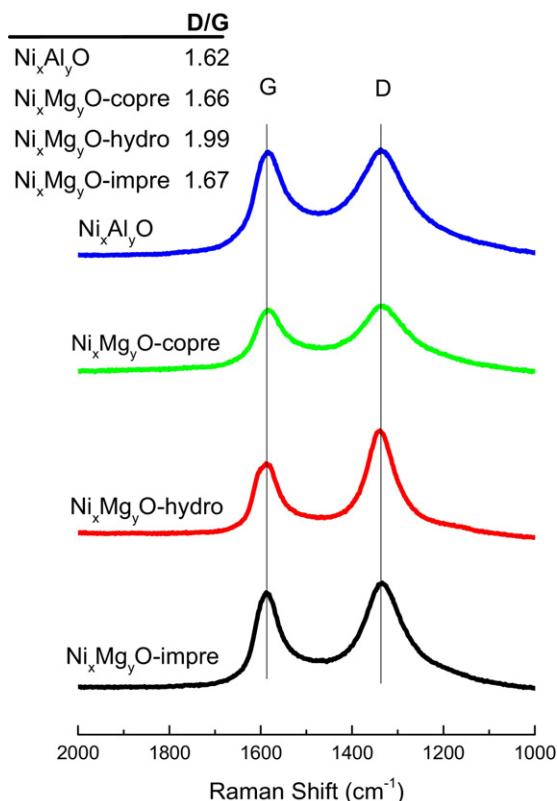[a] ND denotes carbon deposition was not detected.

Fig. 10. Raman spectra of the spent catalysts after 20 h steam reforming (S/C = 1).
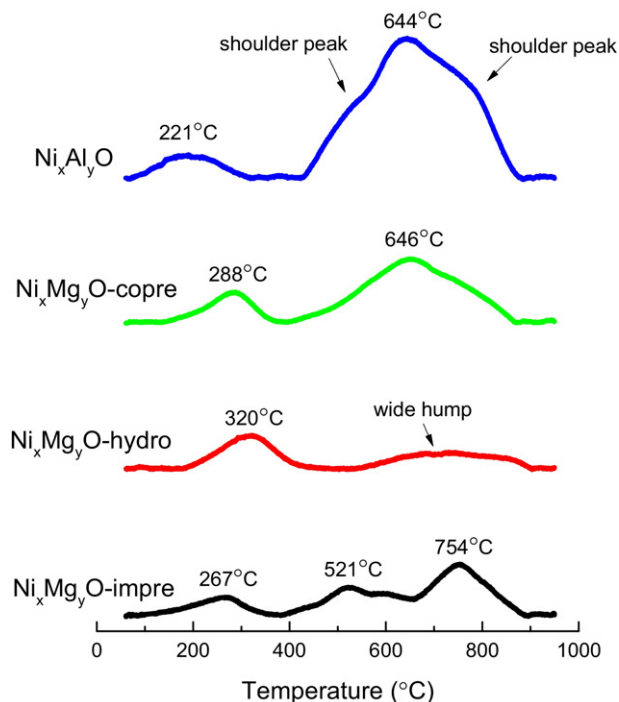

Fig. 11. Temperature programmed hydrogenation profiles for the spent catalysts after 20 h steam reforming (Steam/Carbon = 1).

Four types of carbon species can be identified on the spent Ni_xAl_yO as there were four different hydrogenation temperatures, i.e. two peak temperatures at 221 and 644 °C, and two shoulder peaks at around 500 and 800 °C. It is generally believed [75] that methanol decomposition and CO dissociation were the two main

sources of α-carbon. The main peak at 644 °C represents filamentous carbon (highly ordered, less reactive). Similar carbon species were found on the Ni_xMg_yO-copre catalyst. However, the fraction of β-carbon formed was lower than that of Ni_xAl_yO catalyst.

The first peak identified in Ni_xMg_yO-hydro was for α-carbon. The hump of temperature range at 600–900 °C was due to the existence of both β-carbon and γ-carbon. This small oscillation indicates that a small amount of highly ordered carbon formed on the spent Ni_xMg_yO-hydro, which also confirmed what was found in Raman analysis (Section 3.8.2). The identified hydrogenation peaks for the spent Ni_xMg_yO-impre were similar with those for the spent Ni_xAl_yO, except the missing peak at 644 °C. It is normally believed that deactivation of Ni-impregnated catalysts was associated with the significant amount of inert γ-carbon [78]. The low catalytic performance of both the Ni_xAl_yO and the Ni_xMg_yO-impre at low steam feeding condition was consistent with this TPH test, which showed a significant portion of highly ordered carbon formed on the Ni_xAl_yO and Ni_xMg_yO-impre catalysts.

3.8.4. TEM characterization of spent catalysts

To further investigate the morphology of carbon species deposited on the catalysts, the 4 spent catalysts, after 20 hours' reforming test at S/C = 1, were characterised by using a TEM (as shown in Fig. 12). Carbon species was observed on the spent catalysts, except for Ni_xMg_yO-hydro. Fig. 12(A) and (D) shows carbon filament existed on both Ni_xAl_yO and Ni_xMg_yO-impre catalysts. The formation of such filamentous carbon began with a sufficient amount of dissolved carbon on the rear side of Ni particles [79,80]. When significant amount of carbon deposited on the surface of Ni particles, the access to active sites was blocked and the reforming reaction was inhibited [34,81]. Both the Ni_xAl_yO and the Ni_xMg_yO-impre catalysts showed carbon encapsulation phenomenon (highlighted in Fig. 12), which supported the findings in catalytic reforming that both catalysts exhibited relatively low conversion efficiency after 20 hours' testing. In Fig. 12(B), it can be seen that a large amount of amorphous carbon formed on the Ni_xMg_yO-copre, but most of the Ni particles were still intact within the MgO support and free from encapsulation by carbon deposition. Deactivation of reforming catalysts was also dependent on the type and location of carbon deposition [81,82]. In Fig. 12(B), no carbon was detected on the spent Ni_xMg_yO-hydro at TEM observation, which suggested that the Ni_xMg_yO-hydro was highly resistant to carbon deposition.

The sintering-sensitive nature of the catalysts was also investigated in this study. The average particle size and the size increment of catalysts after 20 hours' reforming at a low steam-to-carbon ratio (S/C = 1) are shown in Table 2. The spent Ni_xMg_yO-copre had the smallest particle size, followed by Ni_xMg_yO-hydro with an average diameter of 15.1 nm. The high resistance to metallic sintering of Ni_xMg_yO-copre could be attributed to its "confined effect", which was mentioned in Section 3.2. The spent Ni_xMg_yO-impre and the spent Ni_xAl_yO catalysts showed an average particle size greater than 20 nm. This result is consistent with the significant deactivation of these two catalysts in low steam-to-carbon ratios as shown in Table 3.

3.8.5. X-ray photoelectron spectra

The oxidation state of Ni species was studied using XPS. The Ni 2p regions of XPS of the fresh and the spent catalysts (after 20 hours' reaction at S/C = 1) were illustrated in Fig. 13. The deconvolution of Ni 2p spectra were carried out by the Gaussian-Lorentzian curve-fitting method. The Ni^{2+} $2p_{3/2}$ was assigned to about 855 and 855.8 eV for the Ni_xMg_yO and the Ni/Al_2O_3, respectively [15,83]. The broad satellite peak was around 7 eV above the main peak of Ni $2p_{3/2}$, which was due to the unscreened $\underline{c}d^8$ and screened $\underline{c}d^{10}\underline{L}^2$ final states [84,85]. Among the fresh catalysts, Ni_xMg_yO-impre was
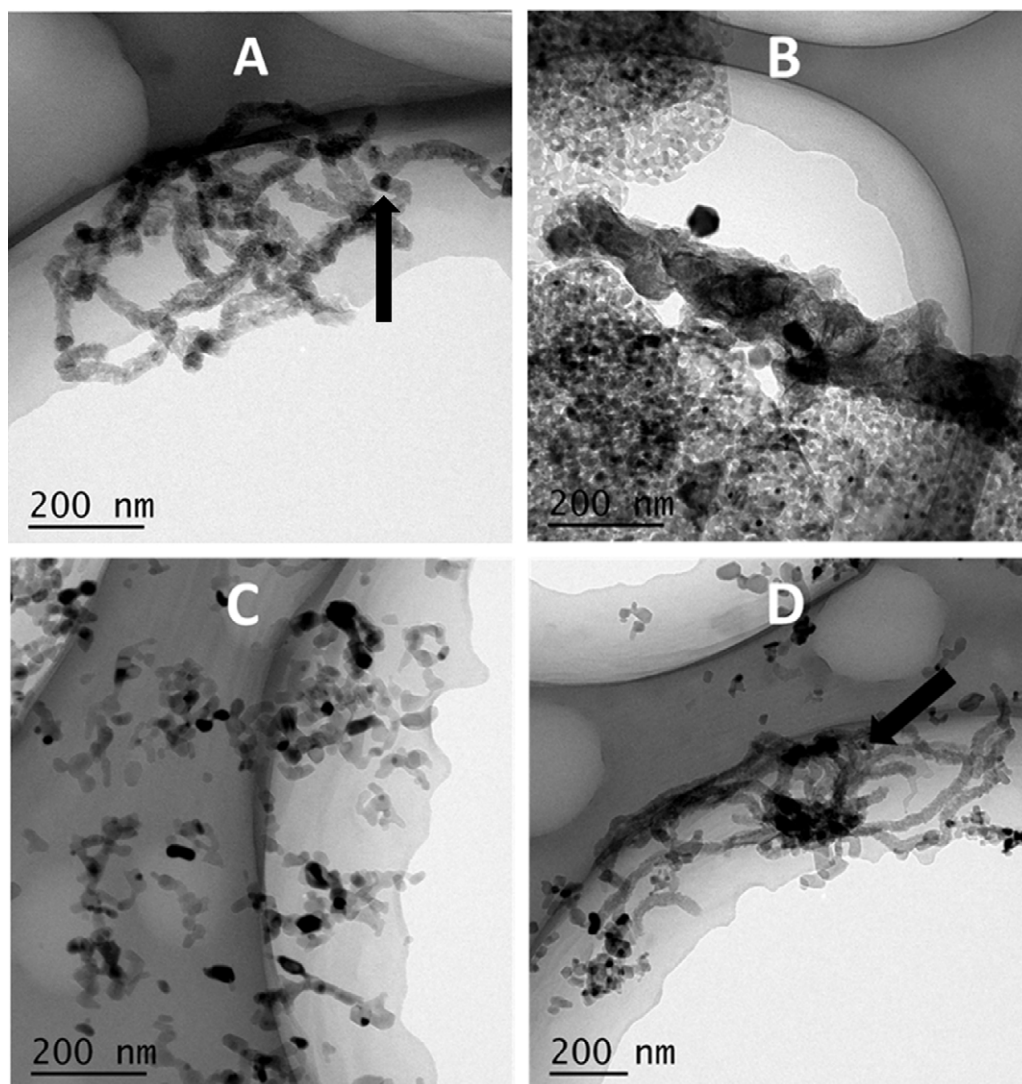
Fig. 12. TEM images for spent catalysts after 20 h steam reaction (S/C = 1) (A) Ni_xAl_yO, (B) Ni_xMg_yO-copre, (C) Ni_xMg_yO-hydro, (D) Ni_xMg_yO-impre.

the only one containing Ni^{3+} at 858.4 eV. The amount of Ni^{3+} on the fresh Ni_xMg_yO-impre was 5.6 times higher than the amount of Ni^{2+}. For the spent Ni_xAl_yO, the nickel particles were not identified on the surface. This might be due to the encapsulation of nickel particles by carbon deposited on the spent catalyst.

Since all the spent catalysts experienced reduction prior to catalytic reforming and were exposed to a strong reducing atmosphere, it was expected that detectable nickel species were all elemental nickel (Ni^0). However, due to these spent catalyst were exposed to air during storage and handling, Ni^0 was oxidized, and Ni^0 (about 852.7 eV) was therefore not identified on the three spent Ni_xMg_yO catalysts, which was consistent with the XRD results (Section 3.1) [15]. Combined with H_2-TPD analysis, it was speculated that most of the Ni particles present at the subsurface of the catalysts, where the oxidized Ni particles were difficult to be reduced at the reaction temperature of 600 °C. Therefore, based on XPS analysis, it can be concluded that different preparation methods resulted in catalysts with different oxidation states of Ni species and therefore different crystal structures.

4. Conclusion

In this research, it is found that catalysts prepared using different preparation methods showed active phase in different crystal structures and nano Ni_xMg_yO solid solutions were found in all the three catalysts studied. The good dispersion of nano-scale Ni species in the Ni_xMg_yO solid solution and the 'isolation effect' of MgO resulted in the formation of nano Ni crystallites in these catalystsafter reduction. A stable catalytic performance of Ni_xMg_yO-hydro (97.4% conversion of methanol and 58.5% hydrogen yield) was maintained for 20 h at a steam-to-carbon ratio of 3. This high catalytic performance was attributed to its nano-scale active phase in the Ni_xMg_yO matrix and its high micropore volume. The excellent anti-carbon deposition capability of this catalyst was attributed to the formation of solid solution that mitigated the agglomeration of Ni particles and the high total basicity of the MgO supports, which supplied sufficient oxygen from the adsorbed CO_2 and H_2O to burn off amorphous carbon.
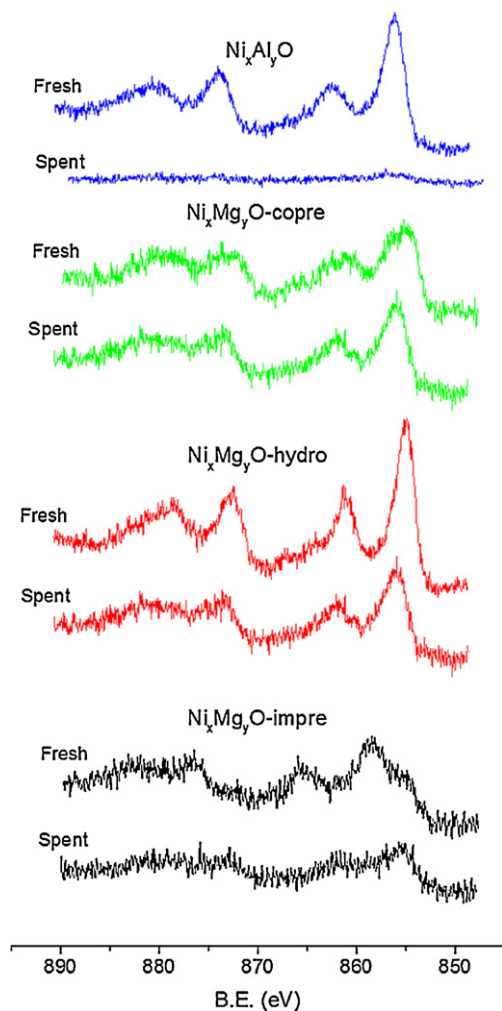
Fig. 13. Ni 2p spectra of the fresh and spent catalsyts.

Acknowledgements

References

[1] C. Song, Catal. Today 115 (2006) 2–32.
[2] A. D'Avignon, F.A. Carloni, E.L.L. Rovere, C.B.S. Dubeux, Energy Policy 38 (2010) 4838–4847.
[3] V.A. Goltsov, T.N. Veziroglu, L.F. Goltsova, Int. J. Hydrog. Energy 31 (2006) 153–159.
[4] F. Zhang, N. Wang, L. Yang, M. Li, L. Huang, Int. J. Hydrog. Energy 39 (2014) 18688–18694.
[5] F. Besenbacher, I. Chorkendorff, B.S. Clausen, B. Hammer, A.M. Molenbroek, J.K. Nørskov, I. Stensgaard, Science 279 (1998) 1913–1915.
[6] C. Rioche, S. Kulkarni, F.C. Meunier, J.P. Breen, R. Burch, Appl. Catal. B—Environ. 61 (2005) 130–139.
[7] F. Chen, C. Wu, L. Dong, A. Vassallo, P.T. Williams, J. Huang, Appl. Catal. B—Environ. 183 (2016) 168–175.
[8] S. Chitsazan, S. Sepehri, G. Garbarino, M.M. Carnasciali, G. Busca, Appl. Catal. B—Environ. 187 (2016) 386–398.
[9] C. He, J. Zheng, K. Wang, H. Lin, J.-Y. Wang, Y. Yang, Appl. Catal. B—Environ. 162 (2015) 401–411.
[10] R.R. Davda, J.W. Shabaker, G.W. Huber, R.D. Cortright, J.A. Dumesic, Appl. Catal. B—Environ. 56 (2005) 171–186.
[11] R.R. Davda, J.W. Shabaker, G.W. Huber, R.D. Cortright, J.A. Dumesic, Appl. Catal. B—Environ. 43 (2003) 13–26.
[12] V. Nichele, M. Signoretto, F. Menegazzo, A. Gallo, V. Dal Santo, G. Cruciani, G. Cerrato, Appl. Catal. B—Environ. 111–112 (2012) 225–232.
[13] H. Ma, L. Zeng, H. Tian, D. Li, X. Wang, X. Li, J. Gong, Appl. Catal. B—Environ. 181 (2016) 321–331.
[14] D.L. Trimm, Catal. Today 37 (1997) 233–238.
[15] M. Yu, K. Zhu, Z. Liu, H. Xiao, W. Deng, X. Zhou, Appl. Catal. B—Environ. 148–149 (2014) 177–190.
[16] K. Yoshida, N. Begum, S.-i. Ito, K. Tomishige, Appl. Catal. A—Gen. 358 (2009) 186–192.
[17] M. García-Diéguez, I.S. Pieta, M.C. Herrera, M.A. Larrubia, L.J. Alemany, J. Catal. 270 (2010) 136–145.
[18] N. Laosiripojana, S. Assabumrungrat, Appl. Catal. A—Gen. 290 (2005) 200–211.
[19] C.-j. Liu, J. Ye, J. Jiang, Y. Pan, ChemCatChem 3 (2011) 529–541.
[20] J. Xu, W. Zhou, J. Wang, Z. Li, J. Ma, Chin. J. Catal. 30 (2009) 1076–1084.
[21] Y.H. Hu, Catal. Today 148 (2009) 206–211.
[22] T. Horiuchi, K. Sakuma, T. Fukui, Y. Kubo, T. Osaki, T. Mori, Appl. Catal. A—Gen. 144 (1996) 111–120.
[23] J.-S. Chang, S.-E. Park, H. Chon, Appl. Catal. A—Gen. 145 (1996) 111–124.
[24] J. Ni, L. Chen, J. Lin, S. Kawi, Nano Energy 1 (2012) 674–686.
[25] W. Hua, L. Jin, X. He, J. Liu, H. Hu, Catal. Commun. 11 (2010) 968–972.
[26] I.H. Son, S. Kwon, J.H. Park, S.J. Lee, Nano Energy 19 (2016) 58–67.
[27] J. Zhang, H. Wang, A.K. Dalai, J. Catal. 249 (2007) 300–310.
[28] F. Arena, F. Frusteri, A. Parmaliana, L. Plyasova, A.N. Shmakov, J. Chem. Soc. Faraday Trans. 92 (1996) 469–471.
[29] Y.H. Hu, E. Ruckenstein, Catal. Lett. 43 (1997) 71–77.
[30] T. Furusawa, A. Tsutsumi, Appl. Catal. A—Gen. 278 (2005) 207–212.
[31] Y.-H. Wang, H.-M. Liu, B.-Q. Xu, J. Mol. Catal. A—Chem. 299 (2009) 44–52.
[32] R.D. Cortright, R.R. Davda, J.A. Dumesic, Nature 418 (2002) 964–967.
[33] V.G. Deshmane, R.Y. Abrokwah, D. Kuila, Int. J. Hydrog. Energy 40 (2015) 10439–10452.
[34] M.-S. Fan, A.Z. Abdullah, S. Bhatia, Appl. Catal. B—Environ. 100 (2010) 365–377.
[35] K. Shi, J. Yan, E. Lester, T. Wu, Ind. Eng. Chem. Res. 53 (2014) 15012–15019.
[36] Z.-Y. Lim, C. Wu, W.G. Wang, K.-L. Choy, H. Yin, J. Mater. Chem. A (2016).
[37] P. Chen, H.-B. Zhang, G.-D. Lin, K.-R. Tsai, Appl. Catal. A—Gen. 166 (1998) 343–350.
[38] S. Tang, J. Lin, K.L. Tan, Catal. Lett. 51 (1998) 169–175.
[39] G. Wu, C. Zhang, S. Li, Z. Han, T. Wang, X. Ma, J. Gong, ACS Sustain. Chem. Eng. 1 (2013) 1052–1062.
[40] A. Al-Ubaid, E.E. Wolf, Appl. Catal. 40 (1988) 73–85.
[41] H. Zhao, X. Luo, J. He, C. Peng, T. Wu, Fuel 147 (2015) 67–75.
[42] T. Xing, L.H. Li, L. Hou, X. Hu, S. Zhou, R. Peter, M. Petravic, Y. Chen, Carbon 57 (2013) 515–519.
[43] D. Li, L. Zeng, X. Li, X. Wang, H. Ma, S. Assabumrungrat, J. Gong, Appl. Catal. B—Environ. 176–177 (2015) 532–541.
[44] K.S.W. Sing, D.H. Everett, R.A.W. Haul, L. Moscou, R.A. Pierotti, J. Rouquerol, T. Siemieniewska, Pure Appl. Chem. 57 (1985) 603–619.
[45] K.W. Sing, J. Porous Mater. 2 (1995) 5–8.
[46] N. Sun, X. Wen, F. Wang, W. Wei, Y. Sun, Energy Environ. Sci. 3 (2010) 366–369.
[47] Z. Liu, R. Che, A.A. Elzatahry, D. Zhao, ACS Nano 8 (2014) 10455–10460.
[48] G. Wu, C. Zhang, S. Li, Z. Huang, S. Yan, S. Wang, X. Ma, J. Gong, Energy Environ. Sci. 5 (2012) 8942–8949.
[49] E.A. Sánchez, M.A. D'Angelo, R.A. Comelli, Int. J. Hydrog. Energy 35 (2010) 5902–5907.
[50] D. Torres, P. Liu, Catal. Lett. 142 (2012) 1211–1217.
[51] S. Wang, G.Q. Lu, Appl. Catal. B—Environ. 19 (1998) 267–277.
[52] K.Y. Koo, H.-S. Roh, Y.T. Seo, D.J. Seo, W.L. Yoon, S.B. Park, Appl. Catal. A—Gen. 340 (2008) 183–190.
[53] K. Zhu, J. Hu, C. Kübel, R. Richards, Angew. Chem. Int. Ed. 118 (2006) 7435–7439.
[54] J. Zhang, H. Wang, A.K. Dalai, Appl. Catal. A—Gen. 339 (2008) 121–129.
[55] S. Wacke, T. Górecki, C. Górecki, K. Książek, JPCS 289 (2011) 012020.
[56] S. Fan, N. Zhao, J. Li, F. Xiao, W. Wei, Y. Sun, Catal. Lett. 120 (2008) 299–302.
[57] Z. Yuan, P. Wu, J. Gao, X. Lu, Z. Hou, X. Zheng, Catal. Lett. 130 (2009) 261–265.
[58] N.S. Babu, R. Sree, P.S.S. Prasad, N. Lingaiah, Energy Fuel 22 (2008) 1965–1971.
[59] O. Bergadà, P. Salagre, Y. Cesteros, F. Medina, J. Sueiras, Catal. Lett. 122 (2008) 259–266.
[60] B. Fidalgo, A. Arenillas, J.Á. Menéndez, Appl. Catal. A—Gen. 390 (2010) 78–83.
[61] S. Patel, K.K. Pant, J. Power Sources 159 (2006) 139–143.
[62] L.-C. Wang, Y.-M. Liu, M. Chen, Y. Cao, H.-Y. He, G.-S. Wu, W.-L. Dai, K.-N. Fan, J. Catal. 246 (2007) 193–204.
[63] L. Gao, G. Sun, S. Kawi, J. Solid State Chem. 181 (2008) 7–13.
[64] S.D. Jones, H.E. Hagelin-Weaver, Appl. Catal. B—Environ. 90 (2009) 195–204.
[65] G. Huang, B.-J. Liaw, C.-J. Jhang, Y.-Z. Chen, Appl. Catal. A—Gen. 358 (2009) 7–12.
[66] N. Laosiripojana, S. Assabumrungrat, J. Power Sources 163 (2007) 943–951.

[67] O.W. Perez-Lopez, A. Senger, N.R. Marcilio, M.A. Lansarin, Appl. Catal. A—Gen. 303 (2006) 234–244.
[68] S. Wang, G.Q.M. Lu, Appl. Catal. B—Environ. 16 (1998) 269–277.
[69] A.I. Tsyganok, T. Tsunoda, S. Hamakawa, K. Suzuki, K. Takehira, T. Hayakawa, J. Catal. 213 (2003) 191–203.
[70] J.R. Rostrup-Nielsen, J. Catal. 33 (1974) 184–201.
[71] J.H. Bitter, K. Seshan, J.A. Lercher, J. Catal. 183 (1999) 336–343.
[72] C. Wu, P.T. Williams, Environ. Sci. Technol. 44 (2010) 5993–5998.
[73] B.M. Vogelaar, A.D. van Langeveld, S. Eijsbouts, J.A. Moulijn, Fuel 86 (2007) 1122–1129.
[74] A.T. Aguayo, P. Castaño, D. Mier, A.G. Gayubo, M. Olazar, J. Bilbao, Ind. Eng. Chem. Res. 50 (2011) 9980–9988.
[75] C.H. Bartholomew, Appl. Catal. A—Gen. 212 (2001) 17–60.
[76] A. Becerra, M. Dimitrijewits, C. Arciprete, A. Castro Luna, Granul. Matter 3 (2001) 79–81.
[77] X.-Y. Quek, D. Liu, W.N.E. Cheo, H. Wang, Y. Chen, Y. Yang, Appl. Catal. B—Environ. 95 (2010) 374–382.
[78] N. Wang, K. Shen, L. Huang, X. Yu, W. Qian, W. Chu, ACS Catal. 3 (2013) 1638–1651.
[79] J. Rostrup-Nielsen, D.L. Trimm, J. Catal. 48 (1977) 155–165.
[80] Y. Liu, Z. Xu, T. Cheng, G. Zhou, J. Wang, W. Li, Y. Bi, K. Zhen, Kinet. Catal. 43 (2002) 522–527.
[81] D. San-José-Alonso, J. Juan-Juan, M.J. Illán-Gómez, M.C. Román-Martínez, Appl. Catal. A—Gen. 371 (2009) 54–59.
[82] P.G. Menon, J. Mol. Catal. 59 (1990) 207–220.
[83] S. Natesakhawat, R.B. Watson, X. Wang, U.S. Ozkan, J. Catal. 234 (2005) 496–508.
[84] M. Oku, K. Hirokawa, J. Elect. Spectrosc. Relat. Phenom. 10 (1977) 103–110.
[85] D. Alders, F.C. Voogt, T. Hibma, G.A. Sawatzky, Phys. Rev. B 54 (1996) 7716–7719.